



Article

Enhanced Thermal Stability of Carbonyl Iron Nanocrystalline Microwave Absorbents by Pinning Grain Boundaries with SiBaFe Alloy Nanoparticles

Yifan Xu ¹, Zhihong Chen ^{2,*} , Ziwen Fu ², Yuchen Hu ², Yunhao Luo ², Wei Li ^{3,*} and Jianguo Guan ^{1,3} ¹ School of Materials and Microelectronics, Wuhan University of Technology, Wuhan 430070, China² School of Science, Wuhan University of Technology, Wuhan 430070, China³ State Key Laboratory of Advanced Technology for Materials Synthesis and Processing, Wuhan University of Technology, Wuhan 430070, China

* Correspondence: z_chen@whut.edu.cn (Z.C.); wellee@whut.edu.cn (W.L.)

Abstract: Nanocrystalline carbonyl iron (CI) particles are promising microwave absorbents at elevated temperature, whereas their excessive grain boundary energy leads to the growth of nanograins and a deterioration in permeability. In this work, we report a strategy to enhance the thermal stability of the grains and microwave absorption of CI particles by doping a SiBaFe alloy. Grain growth was effectively inhibited by the pinning effect of SiBaFe alloy nanoparticles at the grain boundaries. After heat treatment at 600 °C, the grain size of CI particles increased from ~10 nm to 85.1 nm, while that of CI/SiBaFe particles was only 32.0 nm; with the temperature rising to 700 °C, the grain size of CI particles sharply increased to 158.1 nm, while that of CI/SiBaFe particles was only 40.8 nm. Excellent stability in saturation magnetization and microwave absorption was also achieved in CI/SiBaFe particles. After heat treatment at 600 °C, the flaky CI/SiBaFe particles exhibited reflection loss below –10 dB over 7.01~10.11 GHz and a minimum of –14.92 dB when the thickness of their paraffin-based composite was 1.5 mm. We provided a low-cost and efficient kinetic strategy to stabilize the grain size in nanoscale and microwave absorption for nanocrystalline magnetic absorbents working at elevated temperature.

Keywords: magnetic particles; grain size; thermal stability; pinning effect; microwave absorption

Citation: Xu, Y.; Chen, Z.; Fu, Z.; Hu, Y.; Luo, Y.; Li, W.; Guan, J. Enhanced Thermal Stability of Carbonyl Iron Nanocrystalline Microwave Absorbents by Pinning Grain Boundaries with SiBaFe Alloy Nanoparticles. *Nanomaterials* **2024**, *14*, 869. <https://doi.org/10.3390/nano14100869>

Academic Editor: Julian Maria Gonzalez Estevez

Received: 16 March 2024

Revised: 9 May 2024

Accepted: 15 May 2024

Published: 16 May 2024



Copyright: © 2024 by the authors. Licensee MDPI, Basel, Switzerland. This article is an open access article distributed under the terms and conditions of the Creative Commons Attribution (CC BY) license (<https://creativecommons.org/licenses/by/4.0/>).

1. Introduction

With the progress in high-power and miniaturized electronic equipment, electromagnetic interference among heated components raises the urgent need for heat-resistant microwave-absorbing materials [1]. Additionally, heat-resistant microwave-absorbing materials are also required to control the radar cross-section (RCS) of hot parts of military devices [1–3]. At present, the widely used heat-resistant absorbents, such as silicon carbide [4], carbon-based composites [4,5], and barium titanate ceramics [6], exhibit excellent oxidation resistance and stable phases, while their microwave absorption mainly relies on dielectric loss, and there are difficulties in tuning permittivity dispersion over frequency [7,8], giving rise to narrow-band absorption and large thickness. In contrast, magnetic metallic absorbents, such as carbonyl iron (CI) [9], FeSiAl [10], FeCo [3], etc., exhibit both magnetic and dielectric loss to microwaves, in which the resonance and working band can be regulated by the composition and morphology [7]. When the grain size of the magnetic absorbents is on the nanoscale, strong inter-grain exchange coupling and consequent high permeability can be achieved [11,12]. Moreover, nanocrystalline magnetic absorbents are promising at elevated temperature due to their high Curie temperature (T_C), e.g., T_C of Fe reaches around 770 °C, which gives rise to the potential to meet microwave absorption at elevated temperature with low thickness [13].

Nanocrystalline carbonyl iron (CI) is a soft magnetic absorbent with high initial permeability and low permittivity, thus exhibiting good reflection loss in the X (8–12 GHz) and Ku (12–18 GHz) bands [14]. However, when nanocrystalline CI powders are used at elevated temperature, they suffer from oxidation and grain instability. The oxidation caused by active chemical properties of component elements can be effectively inhibited by surface coating [10,15] and selected oxidation [16–18]. Nevertheless, the high-energy nanocrystalline grain boundaries can easily migrate and give rise to severe grain growth [19]. For example, the grains of Fe grew from 10 nm at room temperature to about 6 μm after heat treatment at 700 °C in a vacuum [20]. The coarsened grains affected the electromagnetic parameters via eddy current and ferromagnetic exchange. On one hand, a decrease in the amount of grain boundaries will enhance the electrical conductivity and eddy current [8], which leads to an increase in permittivity and decrease in permeability. On the other hand, according to the anisotropy model of random orientation, the initial permeability is inversely proportional to the sixth power of the grain size within the ferromagnetic exchange length [21,22]. Considering that the grain growth deteriorates the impedance matching of heat-resistant nanocrystalline magnetic absorbents, particular emphasis should be placed on stabilizing the grain size to achieve strong microwave absorption at elevated temperature [23].

From a kinetic perspective, curvature-driven migration of the grain boundaries accounts for the grain growth [24]. Chemically ordered crystal structures, such as the Fe_3Si superlattice [25], can inhibit atomic diffusion and, thus, hinder the migration of grain boundaries [26], while their formation in Fe-based alloys is limited to certain elements. The pinning effect has been widely used to stabilize the grains of nanocrystalline particles, such as solute/second-phase dragging [27–29]. The thermal stability of nanocrystalline Fe/10 wt.% Al alloy was investigated as a typical example, which showed that the generation of the AlN and Al_2O_3 phases effectively hindered grain growth from room temperature to 1200 °C [30]. However, these pinning phases, such as oxides [26,29] and nitrides [30], were often coarsened at high temperature and led to the weakened stabilization of grains [28]. Metallic solutes, such as Zr [31] and Cr [27,31], exhibited lower diffusion than Fe and suppressed grain growth, while they easily formed a solid solution with a matrix at elevated temperature, resulting in rapid grain growth. Therefore, an ideal pinning phase ought to have low solid solubility, a coherent interface, and low diffusion rate in the nanocrystalline CI matrix [26].

In this work, we propose a kinetic strategy to stabilize nanograins in CI particles via the pinning effect. In our strategy, the pinning effect of the SiBaFe alloy was introduced to CI particles by ball milling. The significant difference in the atomic radius among Si, Ba, and Fe prevented the formation of a solid solution; meanwhile, Fe in the SiBaFe alloy helped enhance wettability with the Fe matrix and, thus, ensured the thermal stability of Si and Ba. The obtained CI/SiBaFe composite particles exhibited excellent grain thermal stability, the average grain size of which retained 32.0 nm and 40.9 nm instead of 85.1 nm and 158.1 nm in pure CI after annealing at 600 °C and 700 °C, respectively. Consequently, enhanced saturation magnetization, impedance matching, and microwave absorption were achieved at elevated temperature.

2. Materials and Methods

CI particles and SiBaFe alloy powders were purchased from Shaanxi XingHua Chemistry Share Co., Ltd. (Xingping, China) and Anyang GuangSheng Resistant Metallic Material Co., Ltd. (Anyang, China), respectively. Cyclohexane of analytical purity was purchased from Sinopharm Chemical Reagent Co., Ltd. (Shanghai, China), without further purification.

Flaky CI/SiBaFe particles were obtained by a two-step method of wet ball milling and attritor ball milling. Raw CI and SiBaFe powders to a total of 20 g were first added to a milling tank with 400 g of 316L stainless-steel balls and 20 mL of cyclohexane as the process control agent. The mixture was then milled for 80 h, 120 h, and 160 h at 300 r/min.

The CI/SiBaFe powders were collected by a filter followed by drying at 60 °C for 3 h. The CI/SiBaFe powders were then milled in an attritor with 800 g of ZrO₂ balls and 100 mL of cyclohexane for 8 h at rotation rate of 150 r/min. The resultant flaky CI/SiBaFe particles were collected and subsequently dried at 60 °C for 3 h. In this study, different contents of SiBaFe alloy particles were used to prepare CI/SiBaFe particles, i.e., 5 wt.%, 10 wt.%, and 15 wt.%; the resultant samples were then denoted as CI/SiBaFe-5, CI/SiBaFe-10, and CI/SiBaFe-15, respectively. To test the heat resistance of obtained CI/SiBaFe particles, the powders were annealed at 300~700 °C for 1 h in vacuum.

The morphology of CI/SiBaFe powders was investigated by scanning electron microscopy (SEM, Hitachi S-4800, Hitachi, Japan). The compositions were confirmed by energy-dispersive spectroscopy (EDS) attached to SEM. The crystal structure, grain size, and internal strain of CI/SiBaFe particles were characterized by X-ray diffraction (XRD: Cu K α -1.54060 Å, Bruker D8 Advance, Ettlingen, Germany). Vibrating sample magnetometer (VSM, LakeShore 7404S, Carson, CA, USA) was used to measure the static magnetic properties of powders. The oxidation kinetics of flaky CI and CI/SiBaFe particles was investigated by integrated thermal analysis (Netzsch STA449F3, Hanau, Germany). The samples were heated from room temperature to 1000 °C in air at a rate of 10 °C/min. The thermogravimetric (TG) and differential scanning calorimetric (DSC) curves were recorded during the heating process. To characterize the relative complex permittivity (ϵ_r) and permeability (μ_r) of CI/SiBaFe particles, powders were homogeneously dispersed in paraffin with a mass ratio of 3.265:1, and the mixture was then pressed into a coaxial ring shape, with outer and inner diameters of 7 and 3 mm and heights of 2~3 mm, respectively. The electromagnetic parameters ϵ' , ϵ'' , μ' and μ'' of coaxial samples were measured using vector network analyzer (VNA, Keysight N5230A, Santa Rosa, CA, USA).

3. Results and Discussion

Flaky CI/SiBaFe particles were obtained through a two-step method based on wet and attritor ball milling. Figure 1a illustrates the preparation of CI/SiBaFe particles by wet ball milling. As shown in Figure 1b,c, raw CI particles were in a spherical shape with a diameter less than 5 μ m, while raw SiBaFe alloy particles exhibited a large distribution in dimensions and showed angular fragments, with an average diameter much larger than that of CI. The input of milling energy caused the alloying of CI with SiBaFe, and the preliminarily prepared CI/SiBaFe particles exhibited irregular powders instead of spherical or fragmentary (see Figures 1d and S2), accompanied by the refinement of grains (see Figure S3). The effect of SiBaFe contents on the alloying was investigated by XRD, as shown in Figure 1e–g. The raw CI particles mainly consisted of the α -Fe phase (see Figure 1e), while the raw SiBaFe alloy was mainly composed of elemental Si and compounds such as FeSi₂, BaSi₂ and Ba₂Si (see Figure 1f and Figure S1). All CI/SiBaFe particles with varying SiBaFe contents mainly consisted of the α -Fe phase after milling for 160 h (see Figure 1g). No evident diffraction peak of the raw SiBaFe alloy was observed, revealing that the SiBaFe particles were ground to powders and successfully alloyed with CI particles by ball milling. The difference in the atomic radius among Fe (1.26 Å), Si (1.17 Å), and Ba (2.24 Å) prevented the formation of a solid solution, since no evident shift in diffraction peaks was observed. Also, no diffraction peak of oxides was observed due to the isolation of oxygen from the powders by the sealed milling tank. The EDS images (see Figures 1h–j and S4) indicate that the Fe, Si, and Ba elements were uniformly distributed in CI/SiBaFe particles, without evident segregation.

To enhance the initial magnetic permeability, shape anisotropy was introduced to differentiate the out-of-plane and in-plane magnetic anisotropy fields. Subsequent attritor ball milling was thus employed to obtain flaky CI/SiBaFe particles. As shown in Table 1, the detected contents catered to the feeding ratio. For instance, Fe, Si, and Ba occupied 86.53 wt.%, 8.34 wt.%, and 5.13 wt.% (except C and O), respectively, in flaky CI/SiBaFe-15 particles.

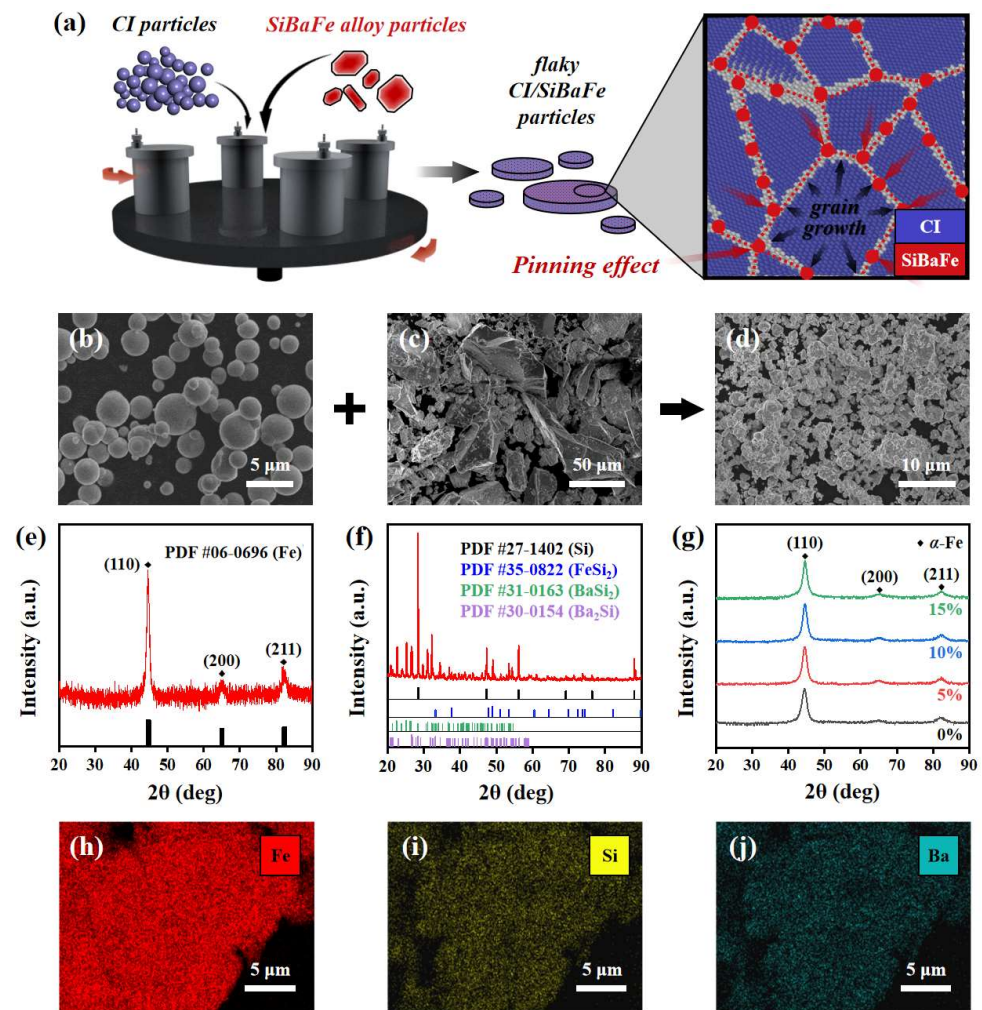


Figure 1. Preparation of CI/SiBaFe particles by wet ball milling: (a) sketch for alloying of CI and SiBaFe particles; (b–d) SEM images of (b) raw CI particles, (c) raw SiBaFe particles, and (d) CI/SiBaFe-15 composite particles; (e–g) XRD spectra of (e) raw CI particles, (f) raw SiBaFe alloy particles, and (g) CI/SiBaFe composite particles with different SiBaFe contents; (h–j) distribution of (h) Fe, (i) Si, and (j) Ba in CI/SiBaFe-15 composite particles.

Table 1. Composition of flaky CI/SiBaFe composite particles.

Sample	Fe (wt.%)	Si (wt.%)	Ba (wt.%)
CI	~100	—	—
CI/SiBaFe-5	94.80 ± 4.95	3.05 ± 1.04	2.15 ± 1.36
CI/SiBaFe-10	90.68 ± 5.18	5.56 ± 1.14	3.76 ± 1.34
CI/SiBaFe-15	86.53 ± 4.67	8.34 ± 1.26	5.13 ± 2.79

To investigate the effect of SiBaFe content on the heat resistance, CI, CI/SiBaFe-5, CI/SiBaFe-10, and CI/SiBaFe-15 were annealed at 300~700 °C for 1 h in a vacuum. The XRD spectra of particles before and after annealing are shown in Figure 2a–d, respectively. The main phase in flaky CI/SiBaFe particles with different SiBaFe contents maintained α -Fe after heat treatment. However, the diffraction peaks exhibited a significant difference in the full width at half maximum (FWHM), indicating variation in the dimensions of grains. The FWHM of the α -Fe diffraction peak was positively correlated with SiBaFe contents, which indicated that SiBaFe doping optimized the grain stability of flaky CI/SiBaFe particles. To

quantify the thermal stability of grains in particles, the corresponding grain size (D) and internal strain (ϵ) of CI/SiBaFe particles were calculated by the Williamson–Hall model [32]:

$$\beta \cos \theta = 4 \sin \theta \cdot \epsilon + \frac{K\lambda}{D} \quad (1)$$

where β is the FWHM, θ is the angle of diffraction peak, λ is the incident wavelength of X-ray equal to 1.54060 Å, and constant K equals 0.89. The results are shown in Figure 2e,f. It can be noticed that the average grain sizes of flaky CI/SiBaFe particles were all about 9 nm at room temperature and did not show an obvious difference after annealing at 300~400 °C, while the growth rate accelerated significantly when the annealing temperature exceeded 500 °C. After annealing at 700 °C, the grain size of CI particles reached 158.10 nm, which increased by 16.8-times compared with 9.38 nm at room temperature. In contrast, the grain size of CI/SiBaFe-15 increased to 40.9 nm, while it was significantly smaller than that of CI. In addition, the internal strain of flaky CI/SiBaFe particles (CI/SiBaFe-5, CI/SiBaFe-10, and CI/SiBaFe-15) decreased with an increase in the annealing temperature, and the decline rate was slightly faster than that of CI particles. A slight increase in ϵ was observed in CI/SiBaFe-15 when the heat treatment exceeded 500 °C, which may have been caused by the different growth rate and local distortion between pinning particles and matrix grains [33]. The variation in grain size and internal strain indicated that the grain growth was effectively hindered by SiBaFe doping.

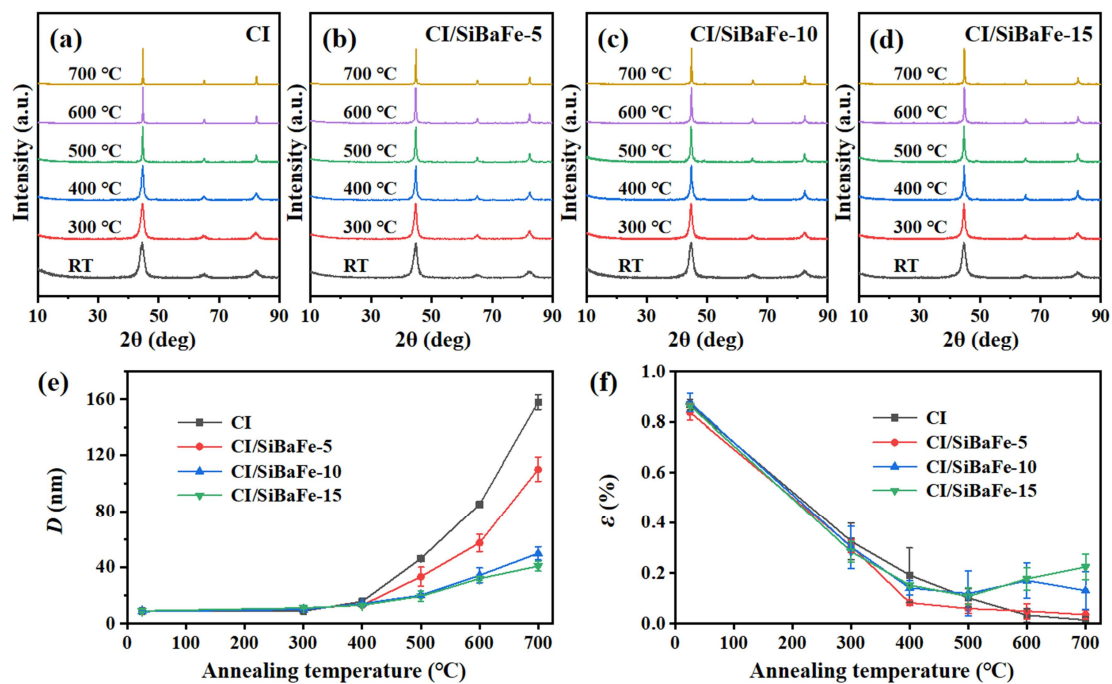


Figure 2. Thermal stability of grains in flaky CI/SiBaFe particles after heat treatment at different temperatures: (a–d) XRD spectra for (a) CI, (b) CI/SiBaFe-5, (c) CI/SiBaFe-10, and (d) CI/SiBaFe-15 particles; (e) grain size; and (f) internal strain.

The superlattice structure in the FeSi alloy after heat treatment has been widely reported [34–36]. However, no superlattice diffraction peak was observed in the XRD spectra of flaky CI/SiBaFe particles. This may have been due to the low SiBaFe contents and the preparation method of ball milling, in which Si and Ba could not easily form a solute with the Fe matrix at the atomic level. No evident shift in the diffraction peaks was observed in the XRD spectra of CI/SiBaFe particles, indicating the absence of a solid solution. Instead, most Si and Ba elements existed at the grain boundaries and did not further dissolve into the α -Fe lattice. From a mechanical perspective, grain boundaries stop migrating when the interfacial tensions from every direction achieve a balance. Pressure

towards the center of curvature at the interface thus generates, which acts positively on the convex grain and negatively on the concave grain. The pressure difference gives rise to the difference in free energy (ΔG) [24]:

$$\Delta G = V_m \Delta p = V_m \gamma \left(\frac{1}{\rho_1} + \frac{1}{\rho_2} \right) \quad (2)$$

where V_m is the molar volume, γ is the surface tension coefficient, and ρ_1 and ρ_2 are the radius of curvature in the convex and concave grains, respectively. The ΔG drives the atoms to transition from the convex to the concave grains, indicating that the migrating tendency of grain boundaries is negatively correlated with the radius of curvature (ρ). Research has revealed that the pinning effect provided by the solutes or second phases inhibits the grain growth by enlarging ρ [26,29,30,37]. Therefore, SiBaFe particles at grain boundaries hindered the displacement of grain boundaries. The optimized thermal stability of grains in flaky CI/SiBaFe particles was closely related to the pinning effect of SiBaFe. Furthermore, previous research indicated that the coherent interface with a matrix, in turn, enhanced the thermal stability of the pinning phases, which required favorable wettability between the two [26,28,30,31]. Otherwise, the grain growth in pinning phases at elevated temperature would severely deteriorate the pinning effect and thermal stability of matrix grains [28]. In flaky CI/SiBaFe particles, Fe from the SiBaFe alloy exhibited excellent wettability with carbonyl iron, which ensured the close integration between the pinning phases and matrix. Therefore, flaky CI/SiBaFe particles exhibited enhanced thermal stability of grains, even after heat treatment at 700 °C.

In addition to grain stability, an anti-oxidation phenomenon was also found after doping SiBaFe in CI. Flaky CI/SiBaFe particles were heated from room temperature to 1000 °C in air, at a rate of 10 °C/min. As shown in Figure 3, the oxidation kinetics of particles was investigated by TG and DSC curves. The results revealed that, with an increase in the SiBaFe contents, the temperature of the weight gain caused by oxidation in flaky CI/SiBaFe particles also gradually increased. For CI particles, their mass reached a maximum of 134.4% at about 450 °C and then barely increased. In a study by Yin et al., flaky CI particles gained a mass of 138.43% after heat treatment in air, which was close to that of Fe₃O₄ in theory [38]. The slightly lower weight gain in our work may be caused by minor impurities or partial oxidation on the surface. Compared with CI, at 450 °C, CI/SiBaFe-5, CI/SiBaFe-10, and CI/SiBaFe-15 exhibited a lower weight gain of 109.30%, 105.43%, and 104.22%, respectively. Although the masses of the samples all increased by about 34% at 1000 °C, the TG curves exhibited a significant difference in the weight-gain tendency. As shown in Figure 3b, the DSC curves revealed that, with an increase in SiBaFe contents, the first endothermic peak gradually shifted from ~401 °C to ~531 °C. In flaky CI/SiBaFe-15 particles, another endothermic peak appeared at ~904 °C. This was because the Si and Ba atoms preferentially bonded with O atoms, since their oxidative activity is superior to Fe [39,40]. At elevated temperature, oxide layers formed due to the oxidation of Si and Ba, which protected CI from interaction with oxygen [15,18]. Inhibition of O diffusion, thus, slowed down the oxidation, and the second endothermic peaks in CI/SiBaFe-10 and CI/SiBaFe-15 may have been caused by the oxidation of Fe after Si drained.

The effect of SiBaFe doping on the static magnetic properties of flaky CI/SiBaFe particles is shown in Figure 4 and Figure S5. In Figure 4a, except for the slight increase at temperatures below 300 °C, the saturation magnetization (M_S) of CI exhibited a significant drop after heat treatment and only retained 71.49 emu/g when the temperature reached 700 °C. The internal strain induced by milling was first released, while the severe grain growth during heat treatment led to a decrease in the amount of grains with a ferromagnetic exchange length and, thus, weakened the ferromagnetic exchange coupling and the consistency of atomic magnetic moments during magnetization [41]. Consequently, the M_S of CI decreased at elevated temperature. In contrast, as shown in Figure 4b,c, due to the pinning effect of SiBa, the M_S of flaky CI/SiBaFe particles remained basically stable throughout heat treatment and exceeded that of pure CI particles at 500~700 °C. Compared

with CI, doping of non-ferromagnetic SiBaFe led to a gradual decrease in M_S with an increase in the doping content; however, the M_S for SiBaFe particles were stable due to the enhanced thermal stability of grain.

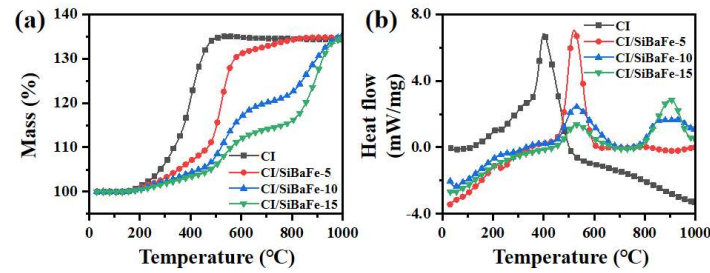


Figure 3. Oxidation kinetics of flaky CI/SiBaFe particles: (a) TG and (b) DSC curves of CI, CI/SiBaFe-5, CI/SiBaFe-10 and CI/SiBaFe-15.

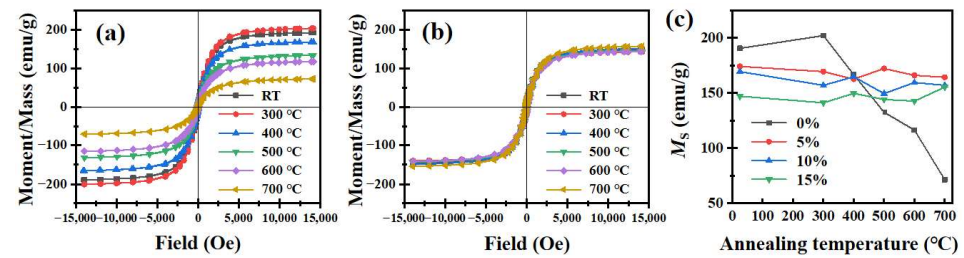


Figure 4. Thermal stability of static magnetic properties of flaky CI/SiBaFe particles: hysteresis loops of (a) CI and (b) CI/SiBaFe-15 before and after heat treatment at different temperature in vacuum; (c) evolution of M_S of flaky CI and CI/SiBaFe particles at different temperature.

Figure 5 exhibits the evolution of the relative complex permittivity ($\epsilon_r = \epsilon' - i\epsilon''$) and complex permeability ($\mu_r = \mu' - i\mu''$) of CI and CI/SiBaFe-15 after heat treatment at different temperatures. As shown in Figure 5a,b, at 1 GHz, the ϵ' of CI particles increased from 21.09 at room temperature to 173.60 at 700 °C, and ϵ'' increased from 2.80 at room temperature to 73.45 at 700 °C. The significant increase in complex permittivity was caused by increased conductivity and enhanced interfacial polarization [8,42]. The relationship between the grain size and volume fraction of grain boundaries (f_{GB}) can be described as [43]:

$$f_{GB} = 1 - \frac{(D - \bar{d})^3}{D^3} \quad (3)$$

where \bar{d} represents the effective thickness of the grain boundary, which is mainly affected by the atomic radius of the alloying element. Since CI contained no other alloying elements, the value of \bar{d} was stable throughout heat treatment. Therefore, grain growth and the consequent decrease in grain boundaries in unit volume reduced electron scattering, resulting in an increase in conductivity and complex permittivity. The accelerated increasing rate of complex permittivity coincided with obvious grain growth when the annealing temperature reached 500 °C. In contrast, the relative complex permittivity of CI/SiBaFe-15 before and after annealing is shown in Figure 5e–f. On one hand, SiBaFe doping reduced the plasticity of composite particles due to the fragility of SiBaFe. The obtained flaky CI/SiBaFe particles exhibited a small average diameter, which reduced the possibility for the formation of a conductive network among particles. On the other hand, low conductivity of the doped Si and Ba led to the weakened electron transport capacity of flaky CI/SiBaFe-15 particles [44–46]. Consequently, the ϵ' and ϵ'' of CI/SiBaFe-15 were significantly lower than that of CI at room temperature. From room temperature to 400 °C, the growth of grains and decrease in defects weakened electron scattering in CI/SiBaFe-15 and accounted for the slight increase in complex permittivity. However, when the annealing temperature exceeded 400 °C, the complex permit-

tivity decreased. The TG and DSC curves shown in Figure 3 indicate the oxidation of Si and Ba. In our heat treatment, air may have reacted with CI/SiBaFe due to the low vacuum. The oxides at grain boundaries weakened the eddy current and exhibited low conductivity [15,18], resulting in a decrease in complex permittivity of over 400 °C.

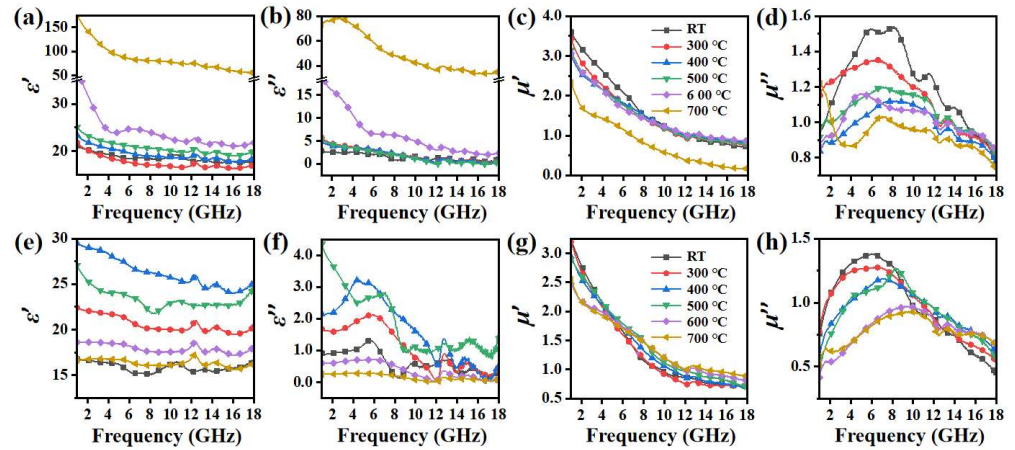


Figure 5. Effects of SiBaFe doping on the thermal stability of electromagnetic parameters: relative complex permittivity and permeability of (a–d) flaky CI and (e–h) CI/SiBaFe-15 particles before and after heat treatment.

As for the relative complex permeability, the results revealed that the real and imaginary parts of the complex permeability of CI both gradually decreased at elevated annealing temperature (see Figure 5c,d). At 1 GHz, the μ' of CI decreased from 3.57 at room temperature to 2.28 at 700 °C, and the maximum of μ'' decreased from 1.54 at room temperature to 0.51 at 700 °C. Considering the exchange coupling among grains, the initial permeability (μ_i) was affected by M_S and D [21,22]:

$$D < L_{\text{ex}}, \mu_i = p_u \frac{M_S^2}{\mu_0 \langle K \rangle} \approx p_u \frac{M_S^2 \cdot A^3}{\mu_0 K_1^4 \cdot D^6} \quad (4a)$$

$$D = L_{\text{ex}}, \mu_i = p_u \frac{M_S^2}{\mu_0 K_1} \quad (4b)$$

$$D > L_{\text{ex}}, \mu_i = p_u \frac{M_S^2 \cdot D}{\mu_0 \sqrt{AK_1}} \quad (4c)$$

where L_{ex} is the ferromagnetic exchange length equal to about 35 nm in Fe-based nanocrystalline [47], $\langle K \rangle$ is the effective anisotropy coefficient, which is proportional to the sixth power of D , K_1 is the magnetocrystalline anisotropy coefficient, μ_0 is permeability in a vacuum, A is the exchange coefficient, and p_u is a constant. Equation (4) indicates that the permeability first rapidly decreased with grain growth within a critical grain size and then changed significantly. According to Equation (4a), the average grain size of CI was retained within the exchange length after heat treatment at 400 °C (~15.8 nm), giving rise to the enlarged magnetocrystalline anisotropy and the rapid decrease in permeability. When the annealing temperature exceeded 500 °C, the average grain size of CI increased to ~46.2 nm, and the μ'' first increased according to the proportional relationship between μ_i and D in Equation (4c), while experiencing a subsequent decrease due to the variation in M_S and K_1 . During the whole heat treatment, M_S , the quadratic term, which decreased at elevated temperature due to the grain growth and consequently weakened the ferromagnetic exchange coupling, would lead to a significant decrease in complex permeability.

The relative complex permeability of CI/SiBaFe-15 is shown in Figure 5g,h. At 1 GHz, μ' decreased from 3.22 at room temperature to 2.52 at 700 °C, and the peak value of μ'' decreased from 1.38 at room temperature to 0.93 at 700 °C, which indicated that both

decrements in the μ' and μ'' of CI/SiBaFe-15 were much smaller than that of CI particles due to the stable grain size. The results revealed that inhibited grain growth by SiBaFe doping helped stabilize the electromagnetic parameters at elevated temperature. The average grain size of CI/SiBaFe-15 was retained far below the exchange length, even after annealing at 500 °C (~19.5 nm), thus exhibiting relatively stable complex permeability. When the annealing temperature exceeded 600 °C, the average grain size gradually increased and reached ~40.9 nm after heat treatment at 600 °C. The consequently weakened ferromagnetic exchange coupling gave rise to a decrease in μ'' .

The reflection loss (RL) and the impedance matching performance of flaky CI and CI/SiBaFe particles were calculated. According to the transmission line theory, the RL, reflectivity from CI/SiBaFe paraffin-based composites, can be calculated by [48]:

$$RL = -20\lg \left| \frac{Z_{in} - Z_0}{Z_{in} + Z_0} \right| \quad (5a)$$

$$Z_{in} = Z_0 \sqrt{\frac{\mu_r}{\epsilon_r}} \tanh \left(j \left(\frac{2\pi ft}{c} \right) \sqrt{\mu_r \epsilon_r} \right) \quad (5b)$$

where Z_0 is the air impedance equal to 377 Ω , Z_{in} and t are the input impedance and thickness of the absorbing material, respectively, and c is the speed of light. The calculated RL when $t = 1.5$ mm is shown in Figure 6a,b. For CI particles, the absorption peak shifted to a lower frequency when heated at elevated temperature, with significant deterioration of the RL, the minimum of which decreased from -13.13 dB at room temperature to -8.60 dB at 600 °C and further to -2.70 dB at 700 °C. In Figure 6c, it can be seen that the increased complex permittivity of CI caused by the growth of grains and removal of defects worsened the impedance matching, resulting in deteriorated microwave absorption at high temperature. For flaky CI/SiBaFe-15 particles, although they exhibited weaker absorption than CI at room temperature, the RL retained stable after heat treatment and was even enhanced at 600~700 °C, which was caused by thermally stable permittivity and magnetic loss. CI/SiBaFe-15 exhibited effective absorption (< -10 dB), ranging from 7.04 to 10.11 GHz at 600 °C, with an increase in the RL minimum from -10.49 dB at room temperature to -14.92 dB. As can be seen in Figure 6d, due to the doping of non-magnetic Si and Ba, CI/SiBaFe-15 exhibited lower permeability and consequent impedance matching. Nevertheless, the grain growth inhibited by the SiBaFe pinning effect cooperated with slight oxidation to inhibit the increase in permittivity when the annealing temperature exceeded 500 °C, thus optimizing the impedance matching. From the calculated results, SiBaFe doping was expected to enhance the microwave absorption of flaky CI/SiBaFe particles at 500~700 °C.

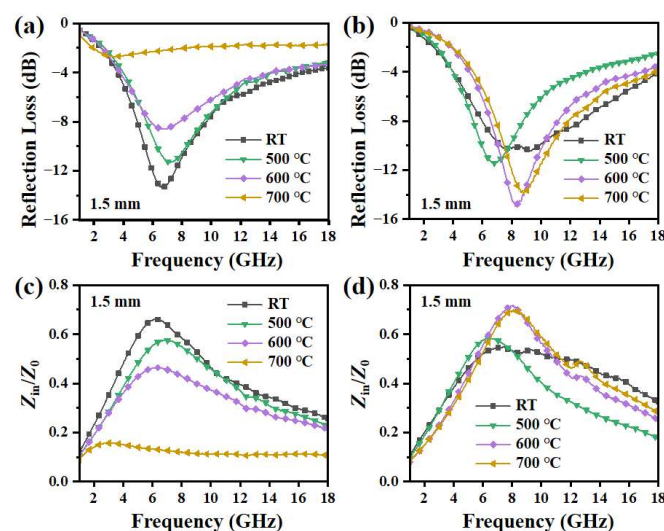


Figure 6. (a,b) Microwave absorption of (a) CI and (b) CI/SiBaFe-15 particles; (c,d) impedance matching analysis for (c) CI and (d) CI/SiBaFe-15 particles.

4. Conclusions

In summary, enhanced microwave absorption at elevated temperature was achieved for flaky CI/SiBaFe particles by inhibiting the grain growth. The SiBaFe alloy was alloyed with carbonyl iron particles via a two-step ball milling method. The pinning phases at the grain boundaries proved to be thermally stable and effectively inhibited the migration of grain boundaries at elevated temperature. The grain size remained at 32.0 nm after annealing at 600 °C and 40.8 nm at 700 °C. The M_S also remained stable after annealing at 300~700 °C due to the ferromagnetic exchange coupling among pinned nanocrystalline grains. After doping at 15 wt.% SiBa, when heated from room temperature to 700 °C, the increment in ϵ' decreased considerably from 152.51 to nearly 0 at 1 GHz, and the decrement in the μ'' maximum decreased from 1.03 to 0.45. The simulated RL of the resultant absorbents in paraffin reached a minimum of -14.92 dB at 1.5 mm and exhibited effective absorption (<-10 dB) with 7.01~10.11 GHz at 600 °C. This work provided an effective route to inhibit grain growth at elevated temperature, and the obtained flaky CI/SiBaFe particles showed great potential for heat-resistant absorbents.

Supplementary Materials: The following supporting information can be downloaded at: <https://www.mdpi.com/article/10.3390/nano14100869/s1>, Figure S1: EDS images of raw SiBaFe alloy particles; Table S1: Composition (except C and O) of SiBaFe alloy particles; Figure S2: SEM images of CI, CI/SiBaFe-5 and CI/SiBaFe-10 particles; Figure S3: XRD spectra, grain size and internal strain of CI/SiBaFe-15 particles before and after milling for different times; Figure S4: SEM images of flaky CI, CI/SiBaFe-5, CI/SiBaFe-10 and CI/SiBaFe-15 particles after attritor ball milling; Figure S5: EDS images of flaky CI/SiBaFe-5 and CI/SiBaFe-10 particles; Figure S6: Hysteresis loops of flaky CI/SiBaFe-5 and CI/SiBaFe-10 particles before and after heat treatment. Figure S7: Microwave absorption and impedance matching analysis of CI/SiBaFe-5 and CI/SiBaFe-10 particles before and after heat treatment.

Author Contributions: Conceptualization, Z.C., W.L. and J.G.; methodology, Y.X. and Z.F.; validation, Y.X., Z.F., Y.H. and Y.L.; formal analysis, Y.H. and Y.L.; investigation, Z.F. and Y.X.; resources, Z.C. and J.G.; data curation, Z.C. and W.L.; writing—original draft preparation, Y.X. and Z.C.; writing—review and editing, Z.C., W.L. and J.G.; visualization, Y.X.; supervision, Z.C., W.L. and J.G.; project administration, Z.C.; funding acquisition, Z.C. and J.G. All authors have read and agreed to the published version of the manuscript.

Funding: This research was funded by the National Natural Science Foundation of China (Nos. 52071239, 52311530074, 51521001) and the Aeronautical Science Foundation of China (2018ZF65002).

Data Availability Statement: The data presented in this study are available on request from the corresponding author.

Acknowledgments: The authors are thankful for the discussion with Suling Zhao from Wuhan University of Technology about the crystalline structure of samples.

Conflicts of Interest: The authors declare no conflicts of interest.

Nomenclature: D : grain size; ϵ : internal strain; β : FWHM, the full width at half maximum; θ : the angle of diffraction peak; λ : the incident wavelength of X-ray equal to 1.54060 Å; K : a constant equal to 0.89; ΔG : free energy; V_m : the molar volume; γ : the surface tension coefficient; ρ_1, ρ_2 : the radius of curvature in the convex and concave grains; M_S : saturation magnetization; f_{GB} : the volume fraction of grain boundaries; \bar{d} : the effective thickness of grain boundary; ϵ_r : the relative complex permittivity; ϵ', ϵ'' : the real and imaginary part of the relative complex permittivity; μ_r : complex permeability; μ', μ'' : the real and imaginary part of the relative complex permeability; μ_i : the initial permeability; L_{ex} : the ferromagnetic exchange length; $\langle K \rangle$: the effective anisotropy coefficient; K_1 : the magnetocrystalline anisotropy coefficient; μ_0 : the permeability in vacuum; A : the exchange coefficient; p_u : a constant related to the materials; RL : reflection loss; Z_0 : the air impedance equal to 377 Ω; Z_{in} : the input impedance of the absorbing material; t : the thickness of the absorbing material; c : the speed of light.

References

1. Qin, F.; Brosseau, C. A review and analysis of microwave absorption in polymer composites filled with carbonaceous particles. *J. Appl. Phys.* **2012**, *111*, 061301. [[CrossRef](#)]
2. Fu, Z.Y.; Pang, A.M.; Luo, H.; Zhou, K.; Yang, H. Research progress of ceramic matrix composites for high temperature stealth technology based on multi-scale collaborative design. *J. Mater. Res. Technol.* **2022**, *18*, 2770–2783. [[CrossRef](#)]
3. Fu, Z.W.; Chen, Z.H.; Wang, R.; Tao, J.; Xu, L.; Peng, G.; Jin, H.; Wang, Y.; Yao, Z.; Zhou, J. Deformation-Thermal Co-Induced Ferromagnetism of Austenite Nanocrystalline FeCoCr Powders for Strong Microwave Absorption. *Nanomaterials* **2022**, *12*, 2263. [[CrossRef](#)]
4. Liu, J.; Wei, X.F.; Gao, L.L.; Tao, J.; Xu, L.; Peng, G.; Jin, H.; Wang, Y.; Yao, Z.; Zhou, J. An overview of C-SiC microwave absorption composites serving in harsh environments. *J. Eur. Ceram. Soc.* **2023**, *43*, 1237–1254. [[CrossRef](#)]
5. Zhang, C.; Li, X.A.; Shi, Y.N.; Wu, H.; Shen, Y.; Wang, C.; Guo, W.; Tian, K.; Wang, H. Structure Engineering of Graphene Nanocages toward High-Performance Microwave Absorption Applications. *Adv. Opt. Mater.* **2021**, *10*, 2101904. [[CrossRef](#)]
6. Saini, L.; Jani, R.K.; Janu, Y.; Kumar, M.; Patra, M.K.; Dixit, A. Gamma radiation induced microwave absorption properties of Ultra-thin barium titanate (BaTiO₃) ceramic tiles over X-Band (8.2–12.4 GHz). *Ceram. Int.* **2021**, *47*, 22397–22403. [[CrossRef](#)]
7. Pang, H.F.; Duan, Y.P.; Huang, L.X.; Song, L.; Liu, J.; Zhang, T.; Yang, X.; Liu, J.; Ma, X.; Di, J.; et al. Research advances in composition, structure and mechanisms of microwave absorbing materials. *Compos. Part B Eng.* **2021**, *224*, 109173. [[CrossRef](#)]
8. Quan, B.; Liang, X.H.; Ji, G.B.; Cheng, Y.; Liu, W.; Ma, J.; Zhang, Y.; Li, D.; Xu, G. Dielectric polarization in electromagnetic wave absorption: Review and perspective. *J. Alloys Compd.* **2017**, *728*, 1065–1075. [[CrossRef](#)]
9. Wang, F.; Long, C.; Wu, T.L.; Li, W.; Chen, Z.; Xia, F.; Wu, J.; Guan, J. Enhancement of low-frequency magnetic permeability and absorption by texturing flaky carbonyl iron particles. *J. Alloys Compd.* **2020**, *823*, 153827. [[CrossRef](#)]
10. Zhou, L.; Xu, H.; Su, G.X.; Zhao, L.; Wang, H.; Wang, Z.; Li, Z. Tunable electromagnetic and broadband microwave absorption of SiO₂-coated FeSiAl absorbents. *J. Alloys Compd.* **2021**, *861*, 157966. [[CrossRef](#)]
11. Otmane, F.; Triaa, S.; Bergheul, S.; Azzaz, M. Grain Size Influence on Microwave Absorption Properties in Nanocrystalline Fe₄₀Co₆₀. *J. Nano Res.* **2014**, *29*, 49–54. [[CrossRef](#)]
12. Zhou, P.H.; Deng, L.J.; Xie, J.L.; Liang, D. Effects of particle morphology and crystal structure on the microwave properties of flake-like nanocrystalline Fe₃Co₂ particles. *J. Alloys Compd.* **2008**, *448*, 303–307. [[CrossRef](#)]
13. Jarlborg, T.; Peter, M. Electronic structure, magnetism and curie temperatures in Fe, Co and Ni. *J. Magn. Magn. Mater.* **1984**, *42*, 89–99. [[CrossRef](#)]
14. Sista, K.S.; Dwarapudi, S.; Kumar, D.; Sinha, G.R.; Moon, A.P. Carbonyl iron powders as absorption material for microwave interference shielding: A review. *J. Alloys Compd.* **2021**, *853*, 157251. [[CrossRef](#)]
15. Guo, Y.; Jian, X.; Zhang, L.; Mu, C.; Yin, L.; Xie, J.; Mahmood, N.; Dou, S.; Che, R.; Deng, L. Plasma-induced FeSiAl@Al₂O₃@SiO₂ core-shell structure for exceptional microwave absorption and anti-oxidation at high temperature. *Chem. Eng. J.* **2020**, *384*, 123371. [[CrossRef](#)]
16. Long, C.; Xu, B.C.; Han, C.Z.; Chen, Z.; Guan, J. Flaky core-shell particles of iron@iron oxides for broadband microwave absorbers in S and C bands. *J. Alloys Compd.* **2017**, *709*, 735–741. [[CrossRef](#)]
17. Liu, Q.C.; Zi, Z.F.; Zhang, M.; Pang, A.; Dai, J.; Sun, Y. Enhanced microwave absorption properties of carbonyl iron/Fe₃O₄ composites synthesized by a simple hydrothermal method. *J. Alloys Compd.* **2013**, *561*, 65–70. [[CrossRef](#)]
18. Wang, H.Y.; Zhu, D.M.; Zhou, W.C.; Luo, F. Electromagnetic property of SiO₂-coated carbonyl iron/polyimide composites as heat resistant microwave absorbing materials. *J. Magn. Magn. Mater.* **2015**, *375*, 111–116. [[CrossRef](#)]
19. Malow, T.R.; Koch, C.C. Grain growth in nanocrystalline iron prepared by mechanical attrition. *Acta Mater.* **1997**, *45*, 2177–2186. [[CrossRef](#)]
20. Darling, K.A.; Chan, R.N.; Wong, P.Z.; Semones, J.E.; Scattergood, R.O.; Koch, C.C. Grain-size stabilization in nanocrystalline FeZr alloys. *Scr. Mater.* **2008**, *59*, 530–533. [[CrossRef](#)]
21. Herzer, G. Grain structure and magnetism of nanocrystalline ferromagnets. *IEEE Trans. Magn.* **1989**, *25*, 3327–3329. [[CrossRef](#)]
22. Herzer, G. Grain size dependence of coercivity and permeability in nanocrystalline ferromagnets. *IEEE Trans. Magn.* **1990**, *26*, 1397–1402. [[CrossRef](#)]
23. Qing, Y.C.; Zhou, W.C.; Jia, S.; Luo, F.; Zhu, D. Effect of Heat Treatment on the Microwave Electromagnetic Properties of Carbonyl Iron/Epoxy-Silicone Resin Coatings. *J. Mater. Sci. Technol.* **2010**, *26*, 1011–1015. [[CrossRef](#)]
24. Hillert, M.; Purdy, G.R. Chemically induced grain boundary migration. *Acta Metall.* **1978**, *26*, 333–340. [[CrossRef](#)]
25. Bansal, C.; Gao, Z.Q.; Fultz, B. Grain growth and chemical ordering in (Fe,Mn)₃Si. *Nanostruct. Mater.* **1995**, *5*, 327–336. [[CrossRef](#)]
26. Peng, H.R.; Gong, M.M.; Chen, Y.Z.; Liu, F. Thermal stability of nanocrystalline materials: Thermodynamics and kinetics. *Int. Mater. Rev.* **2016**, *62*, 303–333. [[CrossRef](#)]
27. Muthaiah, V.M.S.; Koch, C.C.; Mula, S. Thermal stability and mechanical properties of Fe-Cr-Zr alloys developed by mechanical alloying followed by spark plasma sintering. *J. Alloys Compd.* **2021**, *856*, 158266. [[CrossRef](#)]
28. Perez, R.J.; Huang, B.; Lavernia, E.J. Thermal stability of nanocrystalline Fe-10 wt.% Al produced by cryogenic mechanical alloying. *Nanostruct. Mater.* **1996**, *7*, 565–572. [[CrossRef](#)]
29. Shan, G.B.; Chen, Y.Z.; Gong, M.M.; Dong, H.; Li, B.; Liu, F. Influence of Al₂O₃ particle pinning on thermal stability of nanocrystalline Fe. *J. Mater. Sci. Technol.* **2018**, *34*, 599–604. [[CrossRef](#)]

30. Huang, B.; Perez, R.J.; Lavernia, E.J. Grain growth of nanocrystalline Fe–Al alloys produced by cryomilling in liquid argon and nitrogen. *Mater. Sci. Eng. A* **1998**, *255*, 124–132. [[CrossRef](#)]
31. Gupta, R.K.; Singh, R.K.; Koch, C.C. Fabrication and oxidation resistance of nanocrystalline Fe₁₀Cr alloy. *J. Mater. Sci.* **2010**, *45*, 4884–4888. [[CrossRef](#)]
32. Williamson, G.K.; Hall, W.H. X-ray line broadening from filed aluminium and wolfram. *Acta Mater.* **1953**, *1*, 22–31. [[CrossRef](#)]
33. Hernández-Negrete, O.; Tsakiroopoulos, P. On the Microstructure and Isothermal Oxidation of Silica and Alumina Scale Forming Si-23Fe-15Cr-15Ti-1Nb and Si-25Nb-5Al-5Cr-5Ti (at.%) Silicide Alloys. *Materials* **2019**, *12*, 1091. [[CrossRef](#)] [[PubMed](#)]
34. Caracas, R.; Wentzcovitch, R. Equation of state and elasticity of FeSi. *Geophys. Res. Lett.* **2004**, *31*, 183–213. [[CrossRef](#)]
35. Gao, Z.Q.; Fultz, B. Thermal stability of Fe₃Si-based nanocrystals. *Hyperfine Interact.* **1994**, *94*, 2213–2218. [[CrossRef](#)]
36. Kudrnovský, J.; Christensen, N.E.; Andersen, O.K. Electronic structures and magnetic moments of Fe_{3+y}Si_{1-y} and Fe_{3-x}V_xSi alloys with DO₃-derived structure. *Phys. Rev. B* **1991**, *43*, 5924–5933. [[CrossRef](#)] [[PubMed](#)]
37. Kotan, H.; Darling, K.A.; Saber, M.; Koch, C.C.; Scattergood, R.O. Effect of zirconium on grain growth and mechanical properties of a ball-milled nanocrystalline FeNi alloy. *J. Alloys Compd.* **2013**, *551*, 621–629. [[CrossRef](#)]
38. Yin, C.L.; Fan, J.M.; Bai, L.Y.; Ding, F.; Yuan, F. Microwave absorption and antioxidation properties of flaky carbonyl iron passivated with carbon dioxide. *J. Magn. Magn. Mater.* **2013**, *340*, 65–69. [[CrossRef](#)]
39. Sarda, C.; Rousset, A. Thermal stability of barium-doped iron oxides with spinel structure. *Thermochim. Acta* **1993**, *222*, 21–31. [[CrossRef](#)]
40. Zhang, N.; Wang, X.; Liu, T.; Xie, J.; Deng, L. Microwave absorbing performance enhancement of Fe₇₅Si₁₅Al₁₀ composites by selective surface oxidation. *J. Appl. Phys.* **2017**, *122*, 105103. [[CrossRef](#)]
41. Butter, K.; Bomans, P.H.H.; Frederik, P.M.; Vroege, G.; Philipse, A. Direct observation of dipolar chains in iron ferrofluids by cryogenic electron microscopy. *Nat. Mater.* **2003**, *2*, 88–91. [[CrossRef](#)]
42. Kang, Y.Q.; Cao, M.S.; Shi, X.L.; Hou, Z.L. The enhanced dielectric from basalt fibers/nickel core-shell structures synthesized by electroless plating. *Surf. Coat. Technol.* **2007**, *201*, 7201–7206. [[CrossRef](#)]
43. Song, H.W.; Guo, S.R.; Hu, Z.Q. A coherent polycrystal model for the inverse Hall-Petch relation in nanocrystalline materials. *Nanostruct. Mater.* **1999**, *11*, 203–210. [[CrossRef](#)]
44. Debord, R.; Euchner, H.; Pishedda, V.; Hanfland, M.; San-Miguel, A.; Mélinon, P.; Pailhès, S.; Machon, D. Isostructural phase transition by point defect reorganization in the binary type-I clathrate Ba_{7.5}Si₄₅. *Acta Mater.* **2021**, *210*, 116824. [[CrossRef](#)]
45. Hübner, J.M.; Akselrud, L.; Schnelle, W.; Burkhardt, U.; Bobnar, M.; Prots, Y.; Grin, Y.; Schwarz, U. High-Pressure Synthesis and Chemical Bonding of Barium Trisilicide BaSi₃. *Materials* **2019**, *12*, 145. [[CrossRef](#)]
46. Suemasu, T.; Usami, N. Exploring the potential of semiconducting BaSi₂ for thin-film solar cell applications. *J. Phys. D Appl. Phys.* **2017**, *50*, 023001. [[CrossRef](#)]
47. Herzer, G. Anisotropies in soft magnetic nanocrystalline alloys. *J. Magn. Magn. Mater.* **2005**, *294*, 99–106. [[CrossRef](#)]
48. Mishra, V.; Puthucheri, S.; Singh, D. Development of Analytical Approach to Fabricate Composites for Microwave Absorption. *IEEE Trans. Magn.* **2017**, *53*, 2800710. [[CrossRef](#)]

Disclaimer/Publisher’s Note: The statements, opinions and data contained in all publications are solely those of the individual author(s) and contributor(s) and not of MDPI and/or the editor(s). MDPI and/or the editor(s) disclaim responsibility for any injury to people or property resulting from any ideas, methods, instructions or products referred to in the content.